2023 62nd IEEE Conference on Decision and Control (CDC)
December 13-15, 2023. Marina Bay Sands, Singapore

# MrDMD-Based Sensor Placement in Distributed Flow Estimation for the Design of the Artificial Lateral Line of an Underwater Robot

Jun Wang, Tongsheng Shen, Dexin Zhao and Feitian Zhang*

*Abstract*— **An artificial lateral line (ALL) is a sensing system that imitates the distributed perception organs of fish and plays a major role in enhancing the flow estimation capability of underwater robots. Whereas various ALLs have been designed and developed, it is still an open question how to better place ALL sensors on underwater robots, especially for those with complex shapes and working in dynamic flow and robot operating conditions. Aiming to answer this question, this paper presents a novel data-driven sensor placement method for ALLs of underwater robots. This method adopts distributed pressure sensors to measure the flow field along the profile or the outermost boundary of an underwater robot, and quantifies the dynamic information embedded within these measurements using multi-resolution dynamic mode decomposition (mrDMD). The sensors are then positioned by optimizing the dynamic flow information to enhance the perception. Compared with existing sensor placement methods, such as observability maximization and exhaustive experimental search, the proposed method focuses on the modes of dynamics variability at various spatio-temporal scales, thus leading to improved sensing ability especially in complex and dynamic flows. In addition, comprehensively considering the sensor placement under different flow and robot operating conditions, the proposed method is expected to provide an optimal solution for the overall sensing performance of the ALL system. To demonstrate the effectiveness of the proposed method, a case study of background flow speed estimation of oscillating underwater robots of different shapes in a uniform flow is presented.**

## I. Introduction

With the increasing exploitation of the ocean, underwater robots have attracted rapidly rising attention in the science and engineering society during the past decades. The demand for aquatic environmental monitoring, mineral exploitation, national defense, etc., has been continuously expanding [1]–[4]. The energy efficiency and the propulsion performance of underwater robots have dramatically increased with the advancement of robotics technology [2], [4], [5]. However, conventional sensing technologies on land and/or in the air, such as LiDAR, imaging sensors, GPS, etc., cannot be used underwater due to the fast attenuation of electromagnetic signals in water. The commonly-used underwater sensing methods are acoustic and visual. However, their applications are limited. Acoustic sensing is susceptible to interference and not environmental friendly to marine creatures [6]. The visual sensing has a constrained field of view and is very sensitive to light while it is mostly dark and murky in underwater [7], [8]. In addition, acoustic and visual sensing is generally unsuitable in small-sized underwater robots due to the large installation space and high energy consumption.

To enhance the underwater sensing capability, researchers have turned to nature for inspiration. They found that the lateral line, one of the critical sensory systems in fish, plays a crucial role in fish's behaviors [9], [10]. By detecting the surrounding pressure distribution and water vibration, the ALL enables fish to perceive these environmental data robust to hydrological, optical, and auditory variations. After this extraordinary finding, researchers started to design and develop numerous bioinspired ALL systems to enhance underwater sensing. Analogous to fish's lateral line that comprises thousands of distributed sensing organs [10], an ALL system typically consists of a number of distributed sensors (mainly pressure sensors). A variety of ALL systems have been designed for different tasks such as background flow sensing, target detection, hydrodynamics estimation, and localization and navigation [11]–[14].

Sensor placement in the ALL system is a non-trivial research question for improving the sensing capability [10], [15]–[17]. Sensors are mostly placed around the head and uniformly along both sides of an underwater robot in existing studies, either imitating fish's lateral line or following one's design intuition. Very limited research has been reported on the sensor placement of the ALLs. Our previous study optimized the placement of sensors based on the observability analysis, focusing on the observation sensitivity mainly under (quasi-) steady flow conditions [15]. On the other hand, existing studies on ALLs generally adopt underwater robots of certain shapes that are easy to model mathematically [18]–[20], however, inapplicable to those of complex shapes in practice.

This paper proposes a data-driven method to optimize the sensor placement of the ALL system for an underwater robot of any shape under dynamic flow and robot operating conditions. To capture the flow field dynamics at various spatio-temporal scales, this paper uses the Koopman operator theory and multi-resolution dynamic mode decomposition (mrDMD) to recursively decompose the pressure measurements collected around the underwater robot. This modal decomposition process is conducted across various flow and robot operating conditions. All the dynamic modes generated form a modal library, which is expected to fully describe

J. Wang (wjun@stu.pku.edu.cn) is with the Department of Advanced Manufacturing and Robotics, College of Engineering, Peking University, Beijing, China, and also with the National Innovation Institute of Defense Technology, Beijing, China.

T. Shen (shents_bj@126.com) and D. Zhao (zhaodx2008@163.com) are with the National Innovation Institute of Defense Technology, Beijing 100071, China.

F. Zhang (feitian@pku.edu.cn) is with the Department of Advanced Manufacturing and Robotics, and the State Key Laboratory of Turbulence and Complex Systems, College of Engineering, Peking University, Beijing 100871, China.

*Send all corresponces to F. Zhang.

the flow in all the operating conditions of interest with the spatial and temporal flow features decoupled [21], [22]. Selecting the sensor positions that capture the most dynamic information embedded within time-scale dependent modes of variability, this paper achieves sensor placement optimization particularly in dynamic flows, which is then tested in a flow sensing case study.

The main contribution of this paper is the novel sensor placement approach that aims to maximize the multi-resolution flow dynamics information collected by the ALL system. The advantages are threefold: (1) the proposed approach is data-driven and easy to implement, unlike the methods that depend on theoretical flow modeling for regular shaped robots, is suitable for underwater robots of arbitrarily complex shapes; (2) the adopted mrDMD algorithm captures flow dynamics and decomposes it into dynamic modes at different temporal and spatial levels, thus leading to the improved sensing capability considering the overall spatio-temporal flow dynamics; (3) the sensor positioning method comprehensively considers different flow and robot operating conditions via constructing a library of dynamic decomposition modes, expected to be scalable and applicable in various sensing tasks.

The remainder of the paper is organized as follows. Section II describes the sensor placement problem of the ALL system of an underwater robot. Section III presents the proposed method for selecting the sensor positions with maximized flow dynamics information using mrDMD decomposition. Section IV presents the case study of flow sensing using the proposed sensor placement strategy. Finally, conclusion remarks are presented in Section V.

## II. PROBLEM FORMULATION

This paper focuses on the optimization problem of distributed sensor placement of the ALL system for underwater robots of arbitrary shapes under various flow and robot operating conditions.

Following flow analysis conventions, we define a two-dimensional coordinate reference frame with the origin located at the center of mass (or the center of geometry) of the underwater robot of interest, the $x$-axis along its longitudinal axis, and $y$-axis generated by the right-hand rule. The profile or outermost boundary of the robot is then described by a closed curve $c(x, y) = 0$ and the sensor positions to be selected belong to a set of points on the curve discretized based on the physical constraits donated by $\{x_j, y_j\}$ s.t. $c(x_j, y_j) = 0$.

The flow speed scalar field around the robot, evaluated at possible sensor positions of the ALL, is represented by a time series of real-valued matrix $\mathbf{U}_i(x_j, y_j)$, where $i = 1, 2, \dots M$, and $M \in \mathbb{Z}^+$ is the total number of discretized time instants of interest; and $j = 1, 2, 3, ...N$, where $N \in \mathbb{Z}^+$ is the total number of discretized points on the closed curve $c(x, y) = 0$. $\mathbf{U}_i(x_j, y_j)$ is defined to be the snapshot at $i$-th time instant referred to as $\mathbf{U}_i$ for the sake of brevity. Each element in $\mathbf{U}_i$ represents the local flow speed at point $(x_j, y_j)$ on the profile or the outermost boundary of the underwater robot at the $i$-th time instant [14].

According to the Koopman operator theory [23], [24], there exists a linear operator that closely approximates the nonlinear flow dynamics. Reshape each snapshot $\mathbf{U}_i$ into a column vector $\mathbf{u}_i = [\mathbf{u}_{1,i}, \mathbf{u}_{2,i}, ...\mathbf{u}_{N,i}]^T$. The time series of flow snapshots $\mathbf{u}_1, \mathbf{u}_2 \dots \mathbf{u}_M$ sampled at a fixed time interval follows a linear dynamical system, i.e.,

$$\mathbf{Y} = \mathbf{A}\mathbf{X} \tag{1}$$

where $\mathbf{A}$ is a finite approximation of the Koopman operator [23], [24], $\mathbf{X} = \begin{bmatrix} \mathbf{u}_1 & \mathbf{u}_2 & \dots & \mathbf{u}_{M-1} \end{bmatrix}$ and $\mathbf{Y} = \begin{bmatrix} \mathbf{u}_2 & \mathbf{u}_3 & \dots & \mathbf{u}_M \end{bmatrix}$.

Concatenating the flow snapshots, we represent the time series of flow measurements with $\mathbf{U} = [\mathbf{u}_1, \mathbf{u}_2, ...\mathbf{u}_M]$ [14]. Each row in $\mathbf{U}$ represents the sensor measurement at a specific location in the flow field at different sampling time instants, while each column represents the flow field snapshot at a given time measured at different locations. The information contained at the position $(x_j, y_j)$ in the history of flow measurement $\mathbf{U}$ is denoted by $\mathbf{I_d}(\mathbf{U})(x_j, y_j)$ which is typically described by statistical quantities such as mean, variance, and entropy. This paper adopts the overall magnitude of spatiotemporal dynamic modes of variability as the measure which will be discussed in detail in the next section.

The sensor placement is then formulated as an optimization problem to find the points $(x_j, y_j)$ along the profile of the robot $c(x_j, y_j) = 0$ that maximize the information $\mathbf{I_d}(\mathbf{U})$ given the total number of the sensors to be used. Without loss of generality, we consider the optimization problem of find the most informative sensor, i.e.,

$$(x_j, y_j) = \underset{j \in \{1,2,...N\}}{\operatorname{argmax}} \mathbf{I_d}(\mathbf{U})(x_j, y_j) \tag{2}$$

subject to the flow dynamics governed by Eq. (1).

## III. METHOD

This section presents the sensor positioning method for the ALL of an underwater robot. First, a data-driven approach, mrDMD captures the dynamic flow modes of spatio-temporal variations. Next, a library of all the possible dynamic modes under various flow and robot conditions of interest is constructed. Finally, the sensor locations are determined via optimization of the dynamics information possibly collected by the given sensors.

### A. Overview of MrDMD

The DMD method has attracted lots of attention in the fluid dynamics field since Peter Schmid first introduced it in 2010 due to its advantages in identifying the dynamics modes in flow [14], [25]–[27]. It is a data-driven generalized dimensionality reduction method that uses time series data to decompose a nonlinear, high-dimensional, or infinite-dimensional dynamical system (flow field) into a linear combination of a finite number of basis modes. Stemming from the Koopman operator theory, DMD uses a set of

dynamic modes related to certain oscillation frequencies or attenuation/growth rates to describe a flow field [14], [28]. In other words, the temporal evolution can be reconstructed as the weighted sum of the DMD modes.The contribution of each DMD mode to dynamic reconstruction changes periodically with time, and the oscillation frequency and growth/decay rate are determined by their relevant DMD eigenvalues [14], [28].

As researchers continue to investigate DMD, more variants have been developed in terms of but not limited to multiscale analysis, control design, and sparse perception. Among them, mrDMD is a newly-developed trending algorithm that performs multiscale analysis (MRA) similarly to the wavelet transform. By combining MRA with DMD, mrDMD separates the spatial and temporal characteristics of the flow dynamics, providing a powerful tool for analyzing the multiscale features in the dynamical flow system [21], [22]. This paper uses mrDMD to analyze and quantify the flow field dynamics and applies it in the determination of the optimal sensor locations.

MrDMD extends the traditional DMD concerning the spatial and temporal multiscale features. MrDMD adopts layered recursive computation similar to wavelet decomposition and characterizes phenomena of multiple time scales and important transient behaviors in nonlinear dynamical systems [21], [22]. To fully capture the flow dynamics around the underwater robot, the selection of the number of snapshots $M$ should include measurement data that reflects both the high frequency and low frequency portion of the system dynamics. The mrDMD algorithm applies recursively to the $M$ snapshots as follows. First, mrDMD decomposes the system into the dynamic modes [21] and extracts the slowest $m_1$ modes, i.e.,

$$\begin{aligned}\mathbf{X}_{\mathrm{mrDMD}}(t) &= \sum_{k=1}^{M} b_k(0)\boldsymbol{\psi}_k^{(1)} \exp\left(\omega_k t\right) \\ &= \sum_{k=1}^{m_1} b_k(0)\boldsymbol{\psi}_k^{(1)} \exp\left(\omega_k t\right) \\ &\qquad (\text{ slow modes }) \\ &+ \sum_{k=m_1+1}^{M} b_k(0)\boldsymbol{\psi}_k^{(1)} \exp\left(\omega_k t\right) \\ &\qquad (\text{ fast modes })\end{aligned} \tag{3}$$

where $b_k(0)$ is the corresponding $k$-th DMD coefficient, $\boldsymbol{\psi}_k^{(1)}$ is the $k$-th DMD spatial mode and $\exp\left(\omega_k t\right)$ is the $k$-th temporal exponential mode [21]. The oscillation frequency of each mode is ranked and the DMD modes are separated into two groups including the low frequency modes of total number $m_1$ and the remaining high frequency modes of total number $M - m_1$.

After romoving the slow modes, the remaining $M - m_1$ fast modes together create a new time series of snapshots

$$\mathbf{X}_{M/2}(t) = \sum_{k=m_1+1}^{M} b_k(0)\boldsymbol{\psi}_k^{(1)} \exp\left(\omega_k t\right). \tag{4}$$

To achieve multi-scale analysis, divide the freshly created snapshot collection into two parts according to time

$$\mathbf{X}_{M/2} = \mathbf{X}_{M/2}^{(1)} + \mathbf{X}_{M/2}^{(2)} \tag{5}$$

The iteration process works by recursively removing slow frequency components and building the new matrices $\mathbf{X}_{M/2}, \mathbf{X}_{M/4}, \mathbf{X}_{M/8}, \ldots$ until the desired level of decomposition is reached [21], [22]. MrDMD decomposition is then expressed as

$$\begin{aligned}\mathbf{X}_{\mathrm{mrDMD}}(t) = &\sum_{k=1}^{m_1} b_k^{(1)}\boldsymbol{\psi}_k^{(1)} \exp\left(\omega_k^{(1)} t\right) \\ &+ \sum_{k=1}^{m_2} b_k^{(2)}\boldsymbol{\psi}_k^{(2)} \exp\left(\omega_k^{(2)} t\right) \\ &+ \sum_{k=1}^{m_3} b_k^{(3)}\boldsymbol{\psi}_k^{(3)} \exp\left(\omega_k^{(3)} t\right) + \cdots\end{aligned} \tag{6}$$

Here, $\boldsymbol{\psi}_k^{(l)}$ is the $k$-th DMD mode at the $l$-th decomposition level, $\omega_k^{(l)}$ is the $k$-th DMD eigenvalue at the $l$-th decomposition level, $b_k^{(l)}$ is the corresponding DMD coefficient. $m_l$ is the total number of slow modes reserved at the $l$-th decomposition level. Compared to standard DMD, mrDMD provides multi-resolution spatial and temporal features of the system [21].

### *B. Flow Modal Library*

This paper uses mrDMD to analyze the distributed pressure measurement data and characterize the dynamic flow around an underwater robot. Creating a library of dynamic modes under different flow and robot operating conditions is essential for a complete representation of the flow dynamics.

The mrDMD decomposition is applied to the flow field around the underwater robot given a certain operating condition $c \in \mathbb{Z}^+$, and all the dynamic modes of the flow are obtained and combined into a matrix

$$\Psi_c = [\psi_1^{(1)}\ \psi_2^{(1)}\ \cdots\ \psi_{k_1}^{(1)}\ \psi_1^{(2)} \cdots\ \psi_{k_2}^{(2)}\ \cdots\ \psi_1^{(L)} \cdots\ \psi_{k_L}^{(L)}] \tag{7}$$

where $L \in \mathbb{Z}^+$ represents the total number of decomposition levels, $k_l \in \mathbb{Z}^+\ (l = 1, 2, \cdots L)$ represents number of modes extracted at level $l$.

Considering all the flow and robot operating conditions of interest, we create a library of dynamic modes that describe the complete spatiotemporal flow features, denoted by $\Phi = [\Psi_1\ \Psi_2\ \Psi_3 \cdots \Psi_C]$, where $C$ represents the total number of the operating conditions of interest.

### *C. Sensor Placement*

The comprehensive consideration of the sensor placement under different operating conditions requires using the modal sets of the flow field in different operating conditions. However, due to the different information contained in each mode of the flow field in different operating conditions, there are significant differences in the values between the sets of modes, and it is impossible to form a modal library directly. To balance the dynamics information embedded in

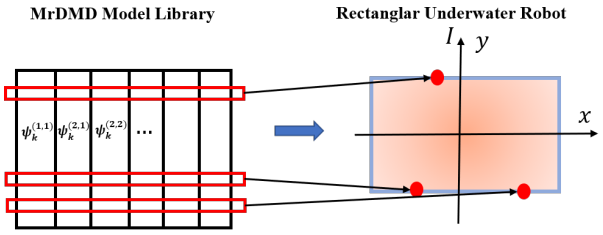


Fig. 1. The schematic of selecting optimal sensor locations based on the constructed mrDMD modal library. The left figure shows the modal library, and the red box represents the selected rows with the top three most flow dynamics information. The right figure shows the profile or outermost boundary of the underwater robots along which the ALL sensors are possibly placed. The red dots represent the selected sensor positions for optimizing flow dynamics information.

the dynamic modes under different operating conditions, it is natural to normalize the mode collection $\Psi_c$. This paper adopts the min-max normalization, i.e.,

$$\Psi_c^n(j,k) = \frac{\Psi_c(j,k) - \min(\Psi_c)}{\max(\Psi_c) - \min(\Psi_c)}. \tag{8}$$

Here $j = 1, 2, 3, ...N$, where $N \in \mathbb{Z}^+$ is the total number of discretized points on the closed curve $c(x, y) = 0$; and $k = 1, 2, \cdots \sum_{l=1}^{L} k_l$, where $\sum_{l=1}^{L} k_l \in \mathbb{Z}^+$ is the total combined number of dynamic modes of the flow at all the decomposition levels; $\max(\cdot)$ and $\min(\cdot)$ represent the maximum and minimum operator, respectively.

To favor some particular operating conditions, the modal library can take different weights accordingly, i.e.,

$$\Phi_w = \left[ s_1\Psi_1^n \;\; s_2\Psi_2^n \;\; \ldots \;\; s_C\Psi_C^n \right]. \tag{9}$$

In this paper, we consider the flow dynamics information captured at a specific sensor location is represented by the time series of measurement data collected at that position. Each row vector of the mode library $\Phi_w$ consists of the coefficients of modes that are decomposed from the time series of measurement data at a certain sensor location. Therefore, to measure the flow dynamics information given a sensor location, we compute the Euclidean norm of the corresponding coefficients over all dynamic modes, or the two-norm of the corresponding row vector of $\Phi_w$. To find the best sensor location that contains possibly the maximum flow dynamics information, we compute the information measure $\mathbf{I_d}(\mathbf{U})(x_j, y_j)$ at all sensor locations $(x_j, y_j)$, where $j = 1, 2, \cdots, N$ by

$$\begin{aligned} \mathbf{I_d}(\mathbf{U}) &= \operatorname{diag}\left(\Phi_w \Phi_w^T\right)^{\frac{1}{2}} \\ &= \left[ ||\Phi_w(1,:)||_2 \;\; ||\Phi_w(2,:)||_2 \;\; \ldots \;\; ||\Phi_w(N,:)||_2 \right]^T \end{aligned} \tag{10}$$

where matrix $\mathbf{I_d}(\mathbf{U})(x_j, y_j)$ consists of all the Euclidean norm of the row vectors of the matrix $\Phi_w$. As shown in Fig. 1, the rows in the modal library matrix represent the flow dynamics at corresponding sensor locations along the profile or the outermost boundary of the underwater robot. The red points have the top three Euclidean norms, indicating that these points contain the most dynamics information in flow. The optimal sensor positions are corresponding to the rows with the maximum Euclidean norms.

This method selects the sensor positions by selecting the rows with the maximum Euclidean norms in the modal library. Therefore, the main computational complexity of this algorithm is on the calculation and sorting of the Euclidean norm of the matrix in terms of its rows. The number of rows represents the number of sensors that are possibly installed on the robot, determined by the dimension of the robot and the selected sensors. Therefore, the size of the flow field determines the number of rows in the modal library, and the number of dynamic modes and operating conditions determine the number of columns. Since, the number of rows is generally far greater than the number of columns, the computational complexity mainly depends on the size of the flow field.

## IV. The Case Study

### A. Simulation Setup

The paper is concerned with sensor placement in various flow conditions for the ALL system of an arbitrarily shaped underwater robot. To demonstrate the effectiveness of the proposed method, a case study is designed which estimates the background flow speed of selected underwater robots.

The case-study experiment uses two shapes, including a rectangle and a triangle to test the adaptability of the proposed method with respect to robots of different shapes. The rectangle is 20 cm long and 12 cm wide. The isosceles triangle is 20 cm high with a base of 12 cm. The background flow is set to 0.4 m/s, 0.5 m/s, 0.6 m/s, 0.7 m/s, respectively, to generate different flow work conditions in terms of the flow speed. In addition, to test the performance of the proposed method when applied to dynamic flow fields, the underwater robots of the two selected shapes will oscillate following a sinusoidal waveform at two oscillation frequencies $f$ of $\frac{9}{\pi}$ Hz and $\frac{9}{2\pi}$ Hz with oscillation amplitudes of $\frac{\pi}{3}$ and $\frac{2\pi}{3}$. The total simulation time is 40 s for all the tests. The method proposed in this paper provides a strategy for selecting the optimal sensor positions given the number of sensors. Without loss of generality, this case study selects five sensors.

The experiment aims to classify the background flow speed based on pressure measurements from these five sensors. While classification methods such as Bayesian and deep neural networks are widely studied these days, considering the limitation of computing resources of underwater robots and the convenience of the classifier training, this paper adopts a traditional decision tree algorithm for the background flow speed estimation. The decision tree uses the direct pressure measurements of the five sensors as input features and the background flow speed as output labels.

### B. Selection of Sensor Locations

The case study simulates the flow using computational fluid dynamics (CFD) for both the rectangular and triangular shaped robots. The pressure measurements around the underwater robot in CFD simulation provide all the data

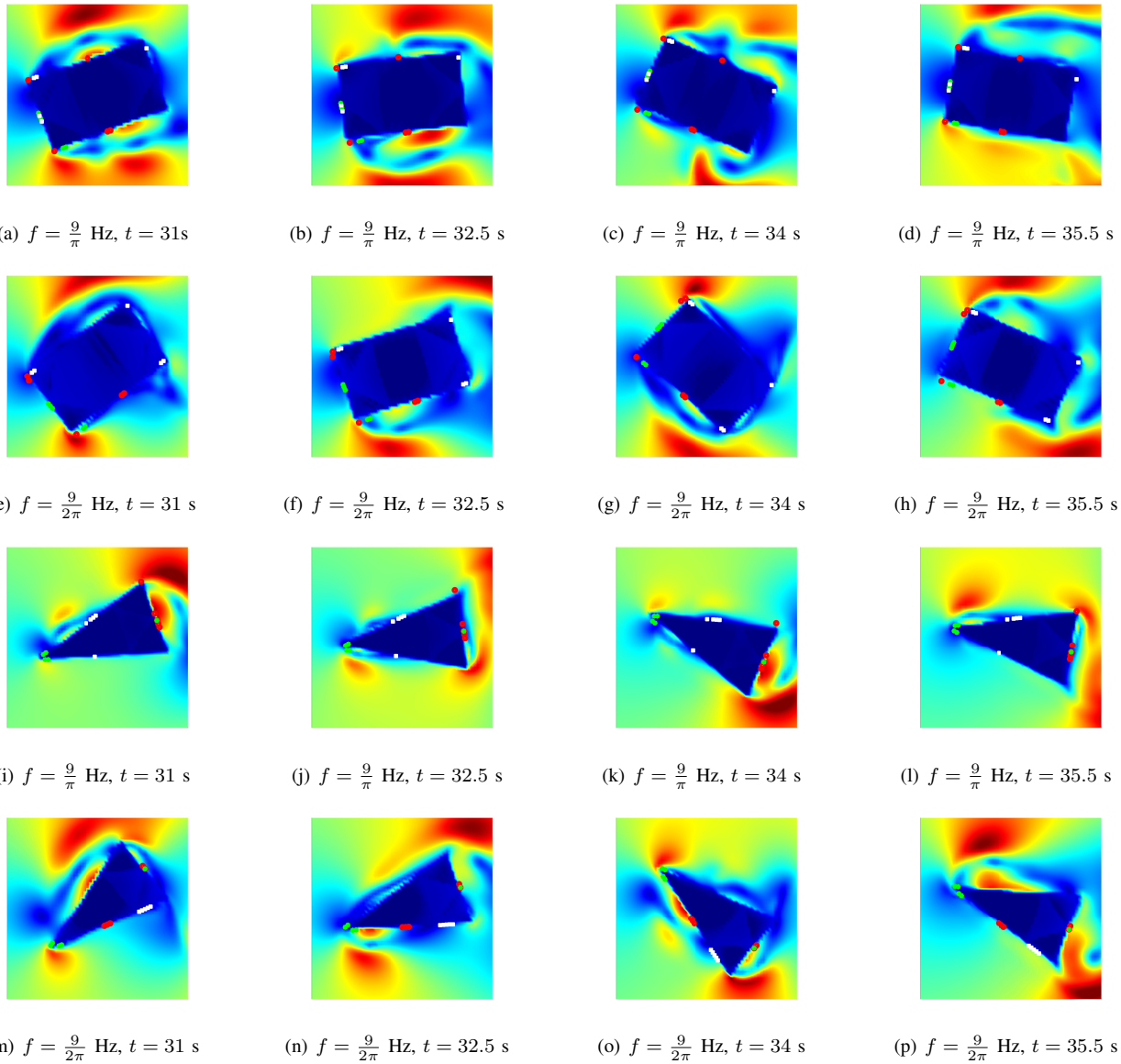

(a) $f = \frac{9}{\pi}$ Hz, $t = 31$s (b) $f = \frac{9}{\pi}$ Hz, $t = 32.5$ s (c) $f = \frac{9}{\pi}$ Hz, $t = 34$ s (d) $f = \frac{9}{\pi}$ Hz, $t = 35.5$ s

(e) $f = \frac{9}{2\pi}$ Hz, $t = 31$ s (f) $f = \frac{9}{2\pi}$ Hz, $t = 32.5$ s (g) $f = \frac{9}{2\pi}$ Hz, $t = 34$ s (h) $f = \frac{9}{2\pi}$ Hz, $t = 35.5$ s

(i) $f = \frac{9}{\pi}$ Hz, $t = 31$ s (j) $f = \frac{9}{\pi}$ Hz, $t = 32.5$ s (k) $f = \frac{9}{\pi}$ Hz, $t = 34$ s (l) $f = \frac{9}{\pi}$ Hz, $t = 35.5$ s

(m) $f = \frac{9}{2\pi}$ Hz, $t = 31$ s (n) $f = \frac{9}{2\pi}$ Hz, $t = 32.5$ s (o) $f = \frac{9}{2\pi}$ Hz, $t = 34$ s (p) $f = \frac{9}{2\pi}$ Hz, $t = 35.5$ s

Fig. 2. Simulation results of sensor placement optimization in background flow estimation using distributed pressure sensors. With the background flow speed set at 0.4 m/s. The first and second rows show the dynamic flow snapshots around the rectangular shape at oscillation frequencies $f$ of $\frac{9}{\pi}$ Hz and $\frac{9}{2\pi}$ Hz, respectively. The third and fourth rows show the dynamic flow snapshots around the triangular shape at oscillation frequencies $f$ of $\frac{9}{\pi}$ Hz and $\frac{9}{2\pi}$ Hz, respectively. The red dots represent the selected optimal sensor positions, the green dots represent the randomly selected sensor positions, and the white dots represent the selected worst sensor positions.

to generate the flow snapshots forming matrices $\mathbf{X}$ and $\mathbf{Y}$ in Eq. (1). Considering practical engineering constraints of sensor installation, the sensor measurement locations are selected with an offset of 0.3 cm away from the profile or the outermost boundary of the robot.

The mrDMD is used to decompose the flow data $\mathbf{X}$ and $\mathbf{Y}$ under different background flow conditions. The coefficients $s_c$ in Eq. (9) are all set equal to 1 in simulation to generate the modal library $\Phi_w$. Finally, by ranking the Euclidean norms of the rows in $\Phi_w$, the sensor positions with the highest measure of dynamic variability are selected. In addition, as comparison trials, we select sensor positions with the lowest measures of dynamic variability that correspond to the smallest Euclidean norms among the rows in $\Phi_w$ as well as the sensor positions randomly selected around the head of the robot following existing studies.

Figure 2 shows the flow snapshots in the case study and the sensor positions selected when the background flow speed is 0.4 m/s. The red dots represent the optimal sensor positions selected based on the proposed sensor placement method, the white dots represent the selected worst sensor positions, and the green dots represent the randomly selected sensor positions. The first and second rows represent the flow snapshots around the rectangular shaped underwater robot when the oscillation frequency $f$ is $\frac{9}{\pi}$ Hz and $\frac{9}{2\pi}$ Hz, respectively. The third and fourth rows represent the flow snapshots around the

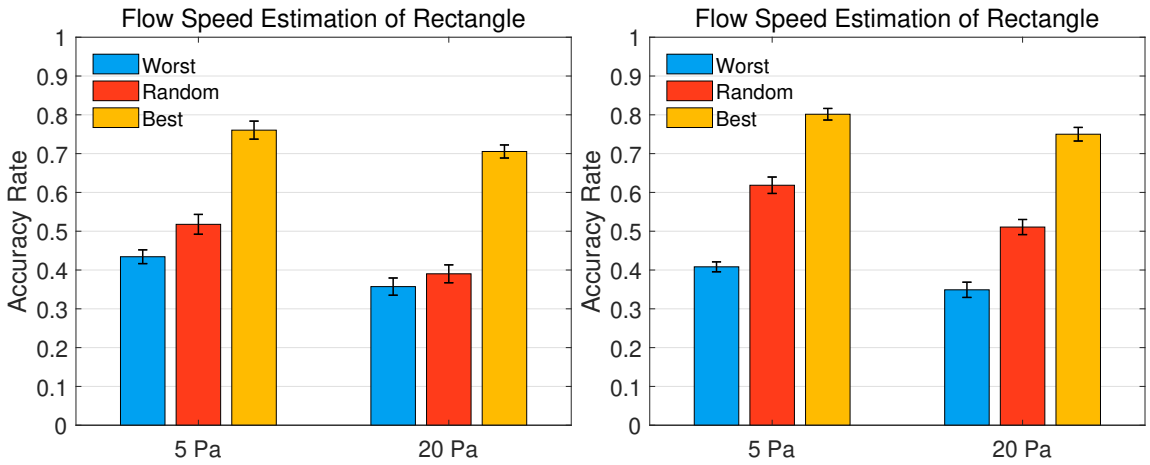


(a) $f = \frac{9}{\pi}$ Hz




(b) $f = \frac{9}{2\pi}$ Hz

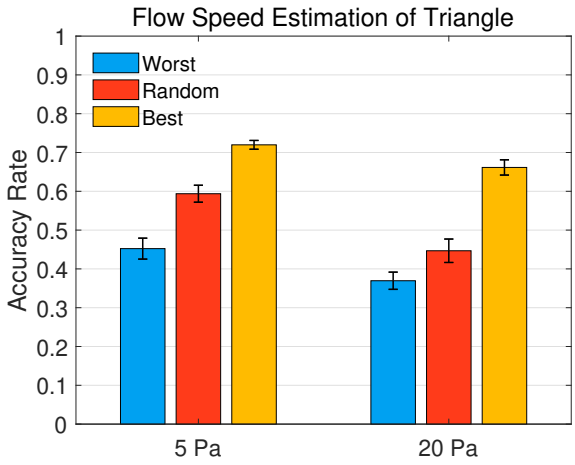


(c) $f = \frac{9}{\pi}$ Hz

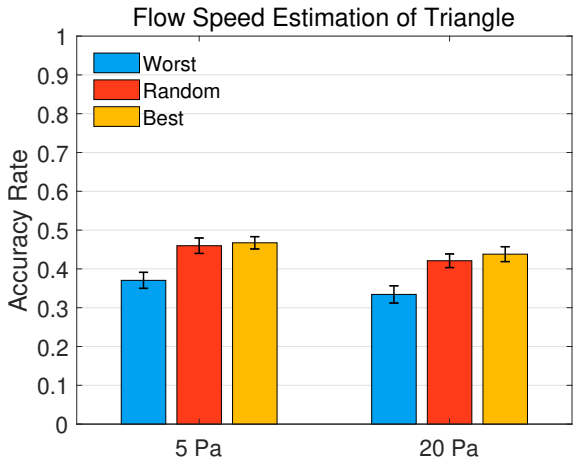


(d) $f = \frac{9}{2\pi}$ Hz

Fig. 3. The statistical estimation results of background flow speed. The first row shows the estimation results of the rectangular robot tested at different oscillation frequencies $f$ of $\frac{9}{\pi}$ Hz and $\frac{9}{2\pi}$ Hz, different background flow speeds at 0.4 m/, 0.5 m/, 0.6 m/, 0.7 m/s, and different level of noise variances of 5 Pa and 20 Pa. The second row represents the estimation results of the triangular robot tested under the same conditions. The blue bar corresponds to the worst sensor positions selected, the red bar corresponds to the randomly selected sensor positions, and the orange bar corresponds to the optimal sensor positions selected.

triangular shaped robot when the oscillation frequency $f$ is $\frac{9}{\pi}$ Hz and $\frac{9}{2\pi}$ Hz, respectively. From the figure, we observe that the flow velocities at the optimal sensor positions have a larger dynamic variation compared to that of the worst and random sensor positions, which is consistent with our design objective.

### C. Background Flow Speed Estimation

Background flow speed estimation is conducted to demonstrate the performance of the selected sensor locations. The data set is from CFD simulation sampled at 10 Hz for 40 s in total. All the 400 data samples have been splitted into the training set and the test set at a ratio of 3 : 1. In addition, we add a Gaussian process noise with mean 0 and a variance of 5 Pa and 20 Pa separately to the pressure data sampled from the CFD simulation. The flow sensing experiments are conducted following combinations of configuration parameters including the robot shapes of triangle and rectangle, the oscillation frequencies of $\frac{9}{\pi}$ Hz and $\frac{9}{2\pi}$ Hz, the noise variance of 5 Pa and 20 Pa, and the background flow speed of 0.4 m/s, 0.5 m/s, 0.6 m/s, 0.7 m/s, with a total number of 32 experimental configurations. Each configuration is repeatedly tested ten times.

Figure 3 shows the statistical results of the 320 experiments. The bar graph represents the averaged accuracy rate over ten repeated experiments at different background speeds. The error bar represents the standard deviation of these experiments. Figures 3(a) and 3(b) present the flow estimation when the rectangular robot oscillates at $\frac{9}{\pi}$ Hz and $\frac{9}{2\pi}$ Hz, respectively. The colors blue, red, and orange correspond to the worst, random, and optimal sensor positions selected based on the proposed optimization approach. Figures 3(c) and 3(d) show the estimation results with the triangular robot.

From Fig. 3, we observe that the optimal sensors selected following the proposed sensor placement method identifies/classifies the background flow velocity at an accuracy rate between 70% and 80% in general, while the randomly

selected sensors lead to an overall estimation accuracy rate between 50% and 60 %, and the worst sensor positions between 40% and 50%. The superior estimation performance by the optimized sensor positions demonstrates that the proposed sensor placement method effectively improves the sensing capability of the ALL system. In addition, based on the standard deviation of the estimation results with respect to the added measurement noise, we consider the performance improvement brought by the optimal sensor placement is consistent.

## V. CONCLUSIONS

In this study, we proposed a data-driven sensor placement strategy for the ALL of an underwater robot. We adopted the mrDMD algorithm to decompose the flow dynamics around the robot into multiscale spatiotemporal modes and ranked the possible sensor positions based on the measure of dynamic variability for the optimization of the sensor locations in terms of the flow dynamics information. This method is expected to be applicable to any underwater robot of an arbitrary shape under various flow/and robot operating conditions. The case-study experiment of background flow estimation was conducted, the results of which validated the proposed sensor placement method.

In future work, we will investigate the influence of the number of sensors on the flow estimation and design an algorithm to select the number that balances the performance and the cost. In addition, we will apply the proposed sensor placement algorithm to the design of the ALL system of the autonomous underwater robot developed in the lab and explore its application in flow-relative navigation and control.

## REFERENCES


[1] M. Kojima, A. Asada, K. Mizuno, K. Nagahashi, F. Katase, Y. Saito, and T. Ura, "AUV IRSAS for submarine hydrothermal deposits exploration," in *2016 IEEE/OES Autonomous Underwater Vehicles (AUV)*, 2016, pp. 161–164.

[2] A. Wolek, T. Gode, C. A. Woolsey, J. Quenzer, and K. A. Morgansen, "Testing a pneumatic underwater glider in shallow water," in *OCEANS 2015 - MTS/IEEE Washington*, 2015, pp. 1–8.

[3] M. Inall, T. Boyd, M. Toberman, C. Old, E. Dumont, and B. Hagan, "AUV observations of surface mixing and bubble entrainment in the clyde estuary, scotland," in *2012 IEEE/OES Autonomous Underwater Vehicles (AUV)*, 2012, pp. 1–4.

[4] F. Zhang, O. Ennasr, E. Litchman, and X. Tan, "Autonomous sampling of water columns using gliding robotic fish: Algorithms and harmful-algae-sampling experiments," *IEEE Systems Journal*, vol. 10, no. 3, pp. 1271–1281, 2016.

[5] P. Phamduy, J. Cheong, and M. Porfiri, "An autonomous charging system for a robotic fish," *IEEE/ASME Transactions on Mechatronics*, vol. 21, no. 6, pp. 2953–2963, 2016.

[6] A. A. Myrberg Jr, "The effects of man-made noise on the behavior of marine animals," *Environment International*, vol. 16, no. 4-6, pp. 575–586, 1990.

[7] M. Lin and C. Yang, "AUV docking method in a confined reservoir with good visibility," *Journal of Intelligent and Robotic Systems*, vol. 100, p. 349–361, 2020.

[8] J. Xu, P. Bi, X. Du, and J. Li, "Robust PCANet on target recognition via the UUV optical vision system," *Optik*, vol. 181, pp. 588–597, 2019.

[9] N. Martiny, S. Sosnowski, K. Kühnlenz, S. Hirche, Y. Nie, J.-M. P. Franosch, and J. L. van Hemmen, "Design of a Lateral-Line sensor for an autonomous underwater vehicle," *IFAC Proceedings Volumes*, vol. 42, no. 18, pp. 292–297, 2009.

[10] Y. Zhai, X. Zheng, and G. Xie, "Fish lateral line inspired flow sensors and flow-aided control: A review," *Journal of Bionic Engineering*, vol. 18, pp. 264–291, 2021.

[11] Y. Xu and K. Mohseni, "A pressure sensory system inspired by the fish lateral line: Hydrodynamic force estimation and wall detection," *IEEE Journal of Oceanic Engineering*, vol. 42, no. 3, pp. 532–543, 2017.

[12] L. D. Chambers, O. Akanyeti, R. Venturelli, J. Ježov, J. Brown, M. Kruusmaa, P. Fiorini, and W. M. Megill, "A fish perspective: detecting flow features while moving using an artificial lateral line in steady and unsteady flow," *Journal of The Royal Society Interface*, vol. 11, no. 99, p. 20140467, 2014.

[13] N. Strokina, J.-K. Kamarainen, J. A. Tuhtan, J. F. Fuentes-Perez, and M. Kruusmaa, "Joint estimation of bulk flow velocity and angle using a lateral line probe," *IEEE Transactions on Instrumentation and Measurement*, vol. 65, no. 3, pp. 601–613, 2016.

[14] F. Dang, S. Nasreen, and F. Zhang, "DMD-based background flow sensing for AUVs in flow pattern changing environments," *IEEE Robotics and Automation Letters*, vol. 6, no. 3, pp. 5207–5214, 2021.

[15] F. Dang and F. Zhang, "Distributed flow estimation for autonomous underwater robots using proper orthogonal decomposition-based model reduction," *Journal of Dynamic Systems, Measurement, and Control*, vol. 141, no. 7, p. 071010, 2019.

[16] Z. Yang, Z. Gong, Y. Jiang, Y. Cai, Z. Ma, X. Na, Z. Dong, and D. Zhang, "Maximized hydrodynamic stimulation strategy for placement of differential pressure and velocity sensors in artificial lateral line systems," *IEEE Robotics and Automation Letters*, vol. 7, no. 2, pp. 2170–2177, 2022.

[17] D. Xu, Z. Lv, H. Zeng, H. Bessaih, and B. Sun, "Sensor placement optimization in the artificial lateral line using optimal weight analysis combining feature distance and variance evaluation," *ISA Transactions*, vol. 86, pp. 110–121, 2019.

[18] A. T. Abdulsadda and X. Tan, "Nonlinear estimation-based dipole source localization for artificial lateral line systems," *Bioinspiration Biomimetics*, vol. 8, no. 2, p. 026005, 2013.

[19] Y. Jiang, Z. Gong, Z. Yang, Z. Ma, C. Wang, Y. Wang, and D. Zhang, "Underwater source localization using an artificial lateral line system with pressure and flow velocity sensor fusion," *IEEE/ASME Transactions on Mechatronics*, vol. 27, no. 1, pp. 245–255, 2022.

[20] B. J. Wolf, S. Warmelink, and S. M. van Netten, "Recurrent neural networks for hydrodynamic imaging using a 2D-sensitive artificial lateral line," *Bioinspiration Biomimetics*, vol. 14, no. 5, p. 055001, 2019.

[21] J. N. Kutz, X. Fu, and S. L. Brunton, "Multiresolution dynamic mode decomposition," *SIAM Journal on Applied Dynamical Systems*, vol. 15, no. 2, pp. 713–735, 2016.

[22] K. Manohar, E. Kaiser, S. L. Brunton, and J. N. Kutz, "Optimized sampling for multiscale dynamics," *Multiscale Model. Simul.*, vol. 17, no. 1, pp. 117–136, 2019.

[23] K. Taira, S. L. Brunton, S. Dawson, C. W. Rowley, T. Colonius, B. J. Mckeon, O. T. Schmidt, S. Gordeyev, V. Theofilis, and L. S. Ukeiley, "Modal analysis of fluid flows: An overview," *AIAA Journal*, vol. 55, no. 12, pp. 4013–4041, 2017.

[24] B. O. Koopman, "Hamiltonian systems and transformation in hilbert space." *Proceedings of the National Academy of Sciences*, vol. 17, no. 5, pp. 315–318, 1931.

[25] K. Menon and R. Mittal, "Dynamic mode decomposition based analysis of flow over a sinusoidally pitching airfoil," *Journal of Fluids and Structures*, vol. 94, p. 102886, 2020.

[26] B. Kramer, P. Grover, P. Boufounos, S. Nabi, and M. Benosman, "Sparse sensing and DMD-Based identification of flow regimes and bifurcations in complex flows," *SIAM Journal on Applied Dynamical Systems*, vol. 16, no. 2, pp. 1164–1196, 2017.

[27] M. Beit-Sadi, J. Krol, and A. Wynn, "Data-driven feature identification and sparse representation of turbulent flows," *International Journal of Heat and Fluid Flow*, vol. 88, p. 108766, 2021.

[28] P. Climaco, J. Garcke, and R. Iza-Teran, "Multi-resolution dynamic mode decomposition for damage detection in wind turbine gearboxes," 2021. [Online]. Available: https://arxiv.org/abs/2110.04103